AARHUS UNIVERSITY

Coversheet

This is the accepted manuscript (post-print version) of the article.
Contentwise, the accepted manuscript version is identical to the final published version, but there may be differences in typography and layout.

How to cite this publication
Please cite the final published version:

Jiawei Zhang, Lirong Song, Aref Mamakhel, Mads Ry Vogel Jørgensen, and Bo Brummerstedt Iversen (2017). High-Performance Low-Cost n-Type Se-Doped Mg3Sb2-Based Zintl Compounds for Thermoelectric Application. In *Chemistry of Materials*, 29 (12), pp 5371–5383
DOI: https://doi.org/10.1021/acs.chemmater.7b01746

Publication metadata

Title:	High-Performance Low-Cost n-Type Se-Doped Mg3Sb2-Based Zintl Compounds for Thermoelectric Application
Author(s):	Jiawei Zhang, Lirong Song, Aref Mamakhel, Mads Ry Vogel Jørgensen, and Bo Brummerstedt Iversen
Journal:	*Chemistry of Materials*
DOI/Link:	https://doi.org/10.1021/acs.chemmater.7b01746
Document version:	Accepted manuscript (post-print)

This document is the Accepted Manuscript version of a Published Work that appeared in final form In *Chemistry of Materials*, 29 (12), pp 5371–5383 DOI: https://doi.org/10.1021/acs.chemmater.7b01746 - copyright © American Chemical Society after peer review and technical editing by the publisher.

General Rights
Copyright and moral rights for the publications made accessible in the public portal are retained by the authors and/or other copyright owners and it is a condition of accessing publications that users recognize and abide by the legal requirements associated with these rights.

- *Users may download and print one copy of any publication from the public portal for the purpose of private study or research.*
- *You may not further distribute the material or use it for any profit-making activity or commercial gain*
- *You may freely distribute the URL identifying the publication in the public portal*

If you believe that this document breaches copyright please contact us providing details, and we will remove access to the work immediately and investigate your claim.

If the document is published under a Creative Commons license, this applies instead of the general rights.

This coversheet template is made available by AU Library
Version 2.0, December 2017

High-performance low-cost n-type Se-doped Mg_3Sb_2-based Zintl compounds for thermoelectric application

Jiawei Zhang,[1] *Lirong Song,*[1] *Aref Mamakhel,*[1] *Mads Ry Vogel Jørgensen,*[1,2] *and Bo Brummerstedt Iversen*[1*]

[1] *Center for Materials Crystallography, Department of Chemistry and iNANO, Aarhus University, DK-8000 Aarhus, Denmark*
[2] *MAX IV Laboratory, Lund, Sweden*
**E-mail:* bo@chem.au.dk

ABSTRACT

Thermoelectric materials, capable of converting heat directly into electricity without moving parts, provide a promising renewable solid-state solution for waste heat harvesting. However, currently available commercial thermoelectric materials PbTe and Bi_2Te_3 are based on tellurium, an extremely scarce and expensive element, which prohibits large scale applications. Herein, we present a systematic study on a new low-cost Te-free material, n-type Se-doped $Mg_3Sb_{1.5}Bi_{0.5}$, by combining the structure and property characterization with electronic structure and electrical transport modelling. Compared with pure Mg_3Sb_2, Se-doped $Mg_3Sb_{1.5}Bi_{0.5}$ shows considerably enhanced power factor as well as much lower thermal conductivity. The excellent electrical transport originates from a nontrivial near-edge conduction band with six conducting carrier pockets and a light conductivity effective mass as well as the weak contribution from a secondary conduction band with a valley degeneracy of 2. The accurate location of the conduction band minimum is revealed from the Fermi surface, which appears to be crucial for the understanding of the electronic transport properties. In addition, the total thermal conductivity is found to be reasonably low (~0.62 W m^{-1} K^{-1} at 725

K). As a result, an optimal zT of 1.23 at 725 K is obtained in $Mg_{3.07}Sb_{1.5}Bi_{0.48}Se_{0.02}$. The high zT, as well as the earth-abundant constituent elements, makes the low-cost Se-doped $Mg_3Sb_{1.5}Bi_{0.5}$ a promising candidate for the intermediate-temperature thermoelectric application. Moreover, the systematic electronic structure and transport modelling provide an insightful guidance for the further optimization of this material and other related Zintl compounds.

INTRODUCTION

More than 50 percent of the energy consumed in producing electricity is lost in the form of waste heat, which is then dissipated into the environment. With the continuous increase of the global energy consumption, developing clean, reliable and sustainable energy solutions has attracted strong worldwide attention. Thermoelectric technology, which enable the direct conversion of waste heat into electricity without moving parts, exhibit great potential in the application of waste heat harvesting.[1] This promising technique, however, is critically hindered by its relatively low efficiency. The thermoelectric conversion efficiency is determined by the dimensionless figure of merit of the material, $zT=\alpha^2\sigma T/\kappa$, where α is the Seebeck coefficient, σ is the electrical conductivity, T is the absolute temperature, and κ is the thermal conductivity.[1,2] Hence, tremendous efforts have been made to improve zT in the past two decades.[3-10] Typically, these efforts can be divided into two main directions: one is to maximize power factor by band structure engineering, such as, band convergence[5,8,10-13] or tuning the electronic states by resonant levels;[4] the other is to reduce the lattice thermal conductivity, for instance, through nanostructuring,[3] alloy scattering[14] or loosely bound rattlers.[15]

Apart from the materials performance, the main obstacle for the widespread application of thermoelectric technology is the high material cost. Currently available commercial thermoelectric materials PbTe and Bi_2Te_3 are based on tellurium, which is an extremely scarce and high-cost element on earth. It is therefore important to explore novel low-cost high-performance materials minimizing or without the use of rare elements. Towards this goal, Mg_3Sb_2-based Zintl compounds can be considered as promising candidates because of their earth abundant, nontoxic, and inexpensive constituent elements. Pure Mg_3Sb_2 is an intrinsic p-type narrow gap semiconductor with a low carrier concentration.[16,17] Accordingly, the poor electrical transport performance of Mg_3Sb_2 limits the overall thermoelectric efficiency, even though it shows reasonably low lattice thermal conductivity. Many efforts, such as orbital engineering[8] and tuning carrier density with a variety of dopants,[18-22] have been devoted to the optimization of p-type performance. In addition, we recently discovered high-performance n-type Te-doped $Mg_3Sb_{1.5}Bi_{0.5}$ with strongly enhanced power factor due to the multi-valley conduction bands.[13] Tamaki *et al.*[23] and Shuai *et al.*[24] reported Te-doped and Nb/Te co-doped $Mg_{3.2}Sb_{1.5}Bi_{0.5}$ by ball milling synthesis, respectively. Ball milling synthesis is prone to introduce impurities such as Fe (from stainless steel milling tools) and carbon (if stearic acid is used as the process control agent), but neither Tamaki *et al.*[23] or Shuai *et al.*[24] reported the actual compositions of the samples. Our synthesis method combines arc melting and spark plasma sintering to produce relatively pure samples showing intrinsic transport properties. Overall, previous reports indicate that n-type Te-doped $Mg_3Sb_{1.5}Bi_{0.5}$ is a promising thermoelectric candidate; however, it will be desirable to develop alternative n-type dopants that are more abundant and cheaper than tellurium.

One attractive alternative is selenium, which is around 50 times more abundant and shows better longe-term price stability than tellurium.[25,26] Here we report a new high-performance n-type $Mg_{3.07}Sb_{1.5}Bi_{0.5}$ thermoelectric material using selenium as an effective electron dopant. In n-type $Mg_{3.07}Sb_{1.5}Bi_{0.48}Se_{0.02}$, a maximum zT of 1.23 at 725 K is obtained, which is at least two times superior to those of p-type Mg_3Sb_2-based compounds such as Ag-doped Mg_3Sb_2,[20] Na-doped Mg_3Sb_2,[19] and $Mg_3Sb_{1.8}Bi_{0.2}$.[22] Considering the abundantly available and low-cost elements, n-type Se-doped $Mg_{3.07}Sb_{1.5}Bi_{0.5}$ is quite promising for thermoelectric applications. At low temperatures, the enhanced zT in Se-doped $Mg_{3.07}Sb_{1.5}Bi_{0.5}$ comes from the combined contribution from the improved power factor and the reduction of the total thermal conductivity. The high zT at high temperatures, however, mainly originates from the strongly enhanced power factor, which is induced by a unique conduction band minimum with six conducting carrier pockets. In addition, the systematic investigation of the electronic structures unravels the accurate location of the six-fold carrier pocket at the conduction band minimum, which appears to be important for the better understanding of the electrical transport. The dominant conduction band minimum with a high valley degeneracy of 6 as well as the weak contribution from a secondary conduction band well describes the electronic transport in n-type $Mg_3Sb_{1.5}Bi_{0.5}$.

EXPERIMENTAL SECTION

Sample synthesis. All samples were prepared by arc melting combined with the spark plasma sintering (SPS) technique. All samples were weighed according to the nominal compositions $Mg_{3.07}Sb_{1.5}Bi_{0.5-x}Se_x$ (x = 0.02, 0.03, 0.04, 0.05, and 0.06). The small amount of the excess Mg was added for the purpose to compensate the Mg evaporation during high-temperature SPS press. High-purity Se shots (>99.999%, Alfa Aesar) were ground into powders (< 100 μm) in an agate mortar. The obtained Se powders together with Sb powders (99.5%, Sigma-Aldrich) and Bi powders (99.9%, Chempur) were weighed and completely mixed in a ball mill mixer (SpectroMill, Chemplex Industries, Inc.) for 15 min. The mixed powders were cold-pressed under uniaxial pressure into dense pellets with approximately 12.7 mm in diameter. The arc melting process was then conducted on the cold-pressed pellets in an argon atmosphere using Edmund Bühler Mini Arc Melting System MAM-1GB. To ensure good homogeneity of the molten ingots, both the top and bottom sides of the pellets were melted twice. The ingots were then crushed and ground into very fine powders with particle sizes smaller than 45 μm in an agate mortar. Mg powders (99.8%, ≤ 44 μm, Alfa Aesar) were weighed in an argon-filled glove box (O_2 and H_2O levels less than 0.1 ppm) and then mixed thoroughly with the obtained powders from the arc-melted ingots in argon in a ball mill mixer for 30 min. Approximately 2 g of the mixed powders were then loaded into a 12.7 mm diameter high-density graphite die protected by the graphite paper in glove box. The mixed powders were sintered by SPS pressing in dynamic vacuum under a pressure of 75 MPa. SPS sintering was conducted using an SPS-515S instrument (SPS Syntex Inc., Japan) by ramping to 823K with a 2 min dwell and then heating to 1123 K for another 4 min.

Structure characterization. Phase purity of the SPS-pressed pellets was checked by X-ray diffraction measurements (XRD) using a Rigaku Smartlab equipped with a Cu Kα_1 source and the standard Bragg-Brentano (BB) optic. The lattice parameters of all samples were obtained by the Fullprof program.[27] The microstructure of the high-performance pellet with x = 0.02 was carried out on FEI Nova Nano SEM 600. High resolution transmission electron microscopy (HRTEM) images and energy dispersive X-ray spectroscopy (EDS) analysis were obtained on FEI TALOS F200A.

In situ XRD. In situ XRD of the high-performance sample with x = 0.02 was carried out on the fresh as-pressed pellet with x = 0.02 using a Rigaku Smartlab equipped with a Co Kα_1 source (wavelength: 1.7889 Å). The sample was placed in an Anton Paar DHS1100 furnace and kept in dynamic vacuum under a graphite dome. The data were collected using a D-tex Ultra detector, and the scan time of 2 min/pattern was used. The pellet was heated from 300 K to 725 K followed by a 5 min dwell and then cooled down to 350 K. For the second cycle, the pellet was heated again to 725 K and then cooled down to 300 K. After the measurement of the bottom surface of the pellet for two thermal cycles, two more thermal cycles were repeated on the top surface. During all these thermal cycles, the heating/cooling rate was 2 K min^{-1}, which is consistent with the Hall measurements.

Thermoelectric transport property measurements. The in-plane resistivity ρ, as well as Hall coefficient (R_H), was measured on the pellets using the *Van der Pauw* method in dynamic vacuum under a magnetic field up to 1.25 T.[28,29] Hall carrier concentration (n_H) was calculated by $1/eR_H$, where e is the elementary charge. The Hall carrier mobility μ_H was then obtained according to the relation $\mu_H = R_H / \rho$. The pellets were annealed by running the resistivity measurement upon heating and cooling for 5 cycles. After the first cycle, the Hall measurements of the pellets are stabilized and consistent in the subsequent 4 heating-cooling cycles (see one example in Figure S1). The resistivity and Hall data of the final cycle was used in the main text. The in-plane Seebeck coefficients of the pellets were then measured from the slope of the thermopower versus temperature gradient using chromel-niobium thermocouples in dynamic vacuum on an in-house system, which has a modified geometry different from the one reported by Iwanaga et al.[30] Although the electrical transport properties show hysteresis between the heating and cooling curves, the hysteresis loop can be well repeated in different cycles (see Figures S1-S3). Moreover, the thermoelectric zT calculated from the heating and cooling curves of different cycles are comparable (see Figure S4). For simplicity, here we use the cooling curves from the final cycle in the main text. The thermal diffusivity (D) from 300 K to 725 K was measured using the laser flash method (Netzsch, LFA457) (Figure S5). Heat capacity (C_P) was indirectly derived using a Pyroceram 9606 standard sample as the reference for the temperature range from 300 to 725 K (Figure S6). The density (d) was measured by the Archimedes method (Table S1). Thermal conductivity was then calculated by $\kappa = dDC_P$. Thermal transport properties showed virtually no hysteresis, thus the heating curve was adopted. The measurement uncertainties typically are 5% for electrical resistivity, 5% for Seebeck coefficient, 5% for thermal diffusivity, 2% for density, 5% for heat capacity, and the combined uncertainty for zT is around 20%.

Density functional theory (DFT) calculations. DFT calculations were carried out using a full-potential linear augmented plane-wave plus local orbitals method as implemented in the Wien2k code.[31] The optimized structure parameters of Mg_3X_2 (X= Sb and Bi) from our previous work[8] were used. The electronic structure calculations by the TB-mBJ potential[32,33] were reproduced from previous work.[13] Band structures were also calculated by the PBE functional[34] for comparison. The situations both with and without spin orbit coupling were considered. The plane wave cut-off parameter $R_{\mathrm{MT}}K_{\mathrm{max}}$ was set to 9. The Brillouin zone was sampled by a dense 36×36×24 k mesh to ensure the well-converged electronic structures. The energy convergence criterion was set to 10^{-4} eV. The Fermi surface was reproduced from previous work[13] using the Xcrysden program.[35]

Using the relaxed structure from previous work,[13] the electronic structure of $Mg_3Sb_{1.5}Bi_{0.5}$ was calculated in a 2×2×2 supercell by PBE functional[34] in VASP code.[36] Band structure of $Mg_3Sb_{1.5}Bi_{0.5}$ was then obtained by unfolding the band structure of the supercell into the primitive cell using the BandUP code.[37,38] Although PBE functional underestimates the band gap, it predicts the correct band topology, which is desirable for the current study. The energy difference between the conduction band minima at the K point and the CB_1 point, labelled $\Delta E_{\text{K-CB}_1}$, and the energy gap E_g of $Mg_3Sb_{2-x}Bi_x$ (x = 0.5, 1, and 1.5) by TB-mBJ potential were calculated from our previous methods[13] by including the energy correction from the accurate conduction band minimum CB_1.

Electrical transport model. Electronic transport properties of n-type Mg_3Sb_2 were simulated by combining the full band structure calculations from mBJ potential with spin orbit coupling and the Boltzmann transport theory under the constant carrier scattering time approximation as implemented in the BoltzTraP code.[39] Moreover, a three band model was used to calculate the electrical transport properties of n-type $Mg_3Sb_{1.5}Bi_{0.5}$ including Seebeck coefficient and power factor at 300 K, 400K, 500 K, and 600 K. The properties were calculated by the conductivity-weighted averages suggested by Putley[40] under the assumption of combined acoustic phonon, alloy, and polar optical phonon scattering for all bands. The input parameters and calculation details of the three band model are provided in Supporting Information.

RESULTS AND DISCUSSION

1. Phase composition and microstructure

XRD patterns of all polycrystalline samples with nominal compositions $Mg_{3.07}Sb_{1.5}Bi_{0.5-x}Se_x$ (x = 0.02-0.06) are shown in Figure 1a. XRD patterns of the top side and bottom side of every sample are consistent with each other and show only minor intensity difference and peak shifting. All major peaks can be well indexed to the low temperature α-Mg_3Sb_2 trigonal phase with a space group of $P\overline{3}m1$ (ICSD #165386). From the enlarged XRD patterns shown in Figure 1b, we found that all samples contain a small amount of MgO, which is likely caused by the slight oxidization during the high-temperature SPS pressing. Moreover, with increasing Se doping content, a small amount of secondary phase can be observed in samples (x = 0.04 and 0.05) and shows a good match to MgSe cubic phase with a space group of $Fm\overline{3}m$ (ICSD #53946). Figure 1c presents the lattice parameters of all compositions. Both lattice parameters a and c show a nearly linear decreasing trend with increasing Se content. This is within our expectation since the ionic radii of Se^{2-} is smaller than that of Bi^{3-}. As the small doping levels of Se, the decrease of lattice constants is minor.

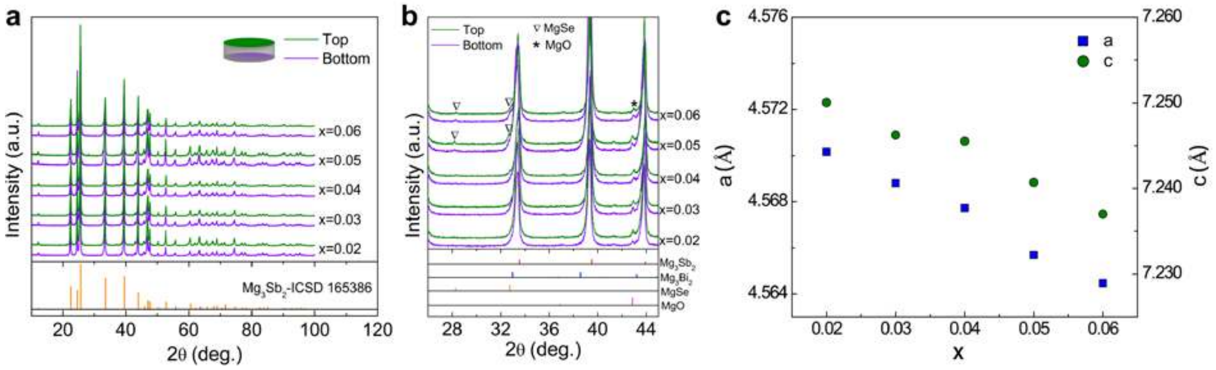

Figure 1. (a) XRD patterns and (b) the enlarged XRD patterns between 26-45° of the top and bottom sides of the pellets with nominal compositions $Mg_{3.07}Sb_{1.5}Bi_{0.5-x}Se_x$ (x = 0.02-0.06). (c) Lattice parameters as a function of the fraction x. The uncertainty is smaller than the size of symbols.

All samples prepared by arc melting followed by SPS pressing show densities at least larger than 90% (Table S1). The SEM images of the fractured cross section and polished surface of the $Mg_{3.07}Sb_{1.5}Bi_{0.48}Se_{0.02}$ sample (Figure 2) confirm the dense sample with no obvious cracks or holes. The detailed microstructure was further investigated on the sample with $x = 0.02$ by TEM. As shown in Figure 3a, the high magnification HRTEM image clearly illustrates three different lattice fringe lines of 0.21 nm, 0.29 nm, and 0.35 nm, which well correspond to the (103), (012), and (011) crystallographic planes, respectively. In addition, the HRTEM graph clearly depicts that several nano-size single crystalline grains with the stacking of the randomly orientated planes. Although the Se doping level in the sample is relatively small, the existence of Se element is confirmed by the peak in the EDS spectrum (Figure 3b). The elemental composition result by TEM-EDS analysis indicates that the actual composition of the $Mg_{3.07}Sb_{1.5}Bi_{0.48}Se_{0.02}$ sample is close to the nominal value. The slightly lower actual Mg content is typically induced by the evaporation of Mg during high-temperature SPS sintering. The EDS elemental mapping was also conducted and is shown in Figure 3c-g. It is clear that Mg, Sb, Bi, and Se atoms are distributed nearly uniformly in the sample.

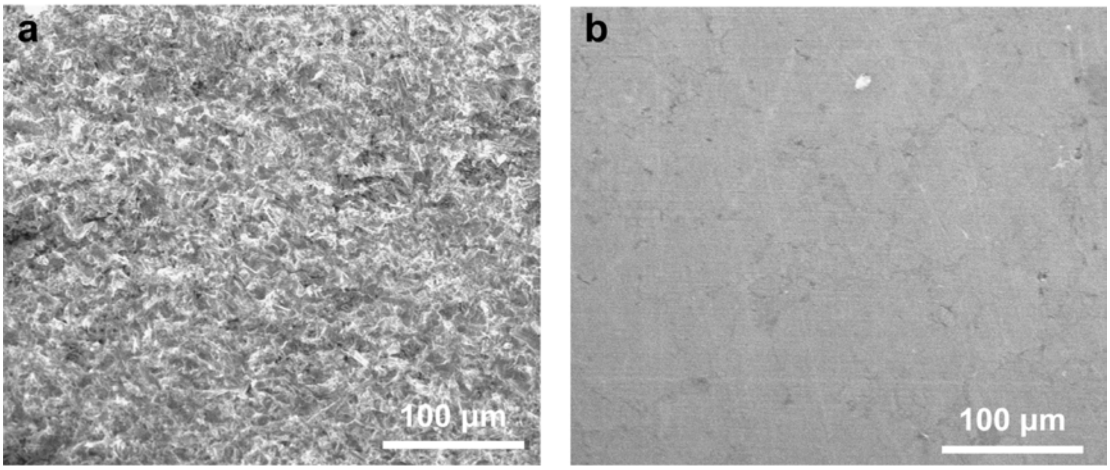

Figure 2. SEM images of (a) the fractured cross section and (b) polished surface of the sample with $x = 0.02$.

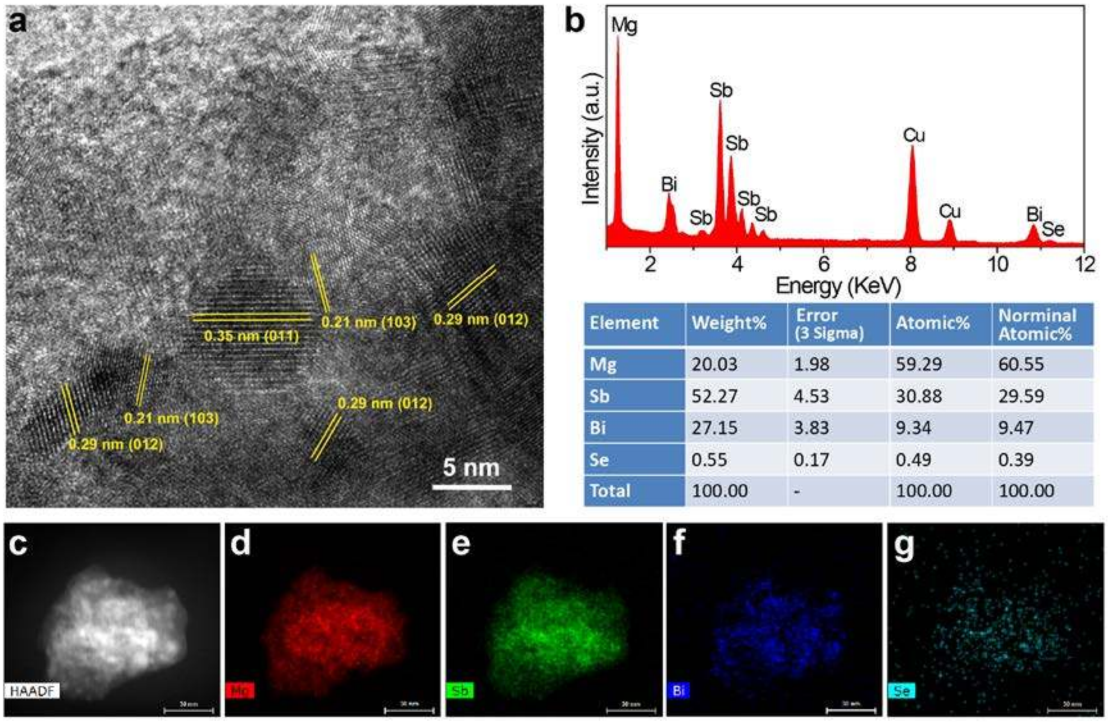

Element	Weight%	Error (3 Sigma)	Atomic%	Norminal Atomic%
Mg	20.03	1.98	59.29	60.55
Sb	52.27	4.53	30.88	29.59
Bi	27.15	3.83	9.34	9.47
Se	0.55	0.17	0.49	0.39
Total	100.00	-	100.00	100.00

Figure 3. (a) High resolution TEM image, (b) EDS spectra with the elemental composition analysis (Cu peaks come from the TEM grid), and (c-g) EDS mapping images of $Mg_{3.07}Sb_{1.5}Bi_{0.48}Se_{0.02}$ sample.

2. Phase stability by in situ XRD

The transport properties of a material usually exhibit a highly nontrivial dependence on phase composition and structure. Diffraction data are often simply used to conduct a quick check of the phase purity; however, this means that any structural changes induced the thermal cycling during the property measurements might be overlooked.[41] It is therefore crucial to study the phase stability under the repeated thermal cycles. Towards this purpose, the *in situ* XRD experiment was carried out on the high performance pellet with $x = 0.02$ for four thermal cycles (two cycles for each side of the pellet). A fresh pellet was used to avoid any thermal history. It should be noted that the temperature profile including the heating/cooling rate of *in-situ* XRD is kept the same as Hall measurements. The result is demonstrated in Figure 4. It is clear that there is no obvious structural change during the four thermal cycles for both the bottom and top surface of the pellet, indicating the high performance sample is thermally stable in bulk form (at least on the surfaces of the pellet). The present in situ data provide an initial assessment of the thermal stability, but a comprehensive study of the thermal stability will be carried out in our future work.

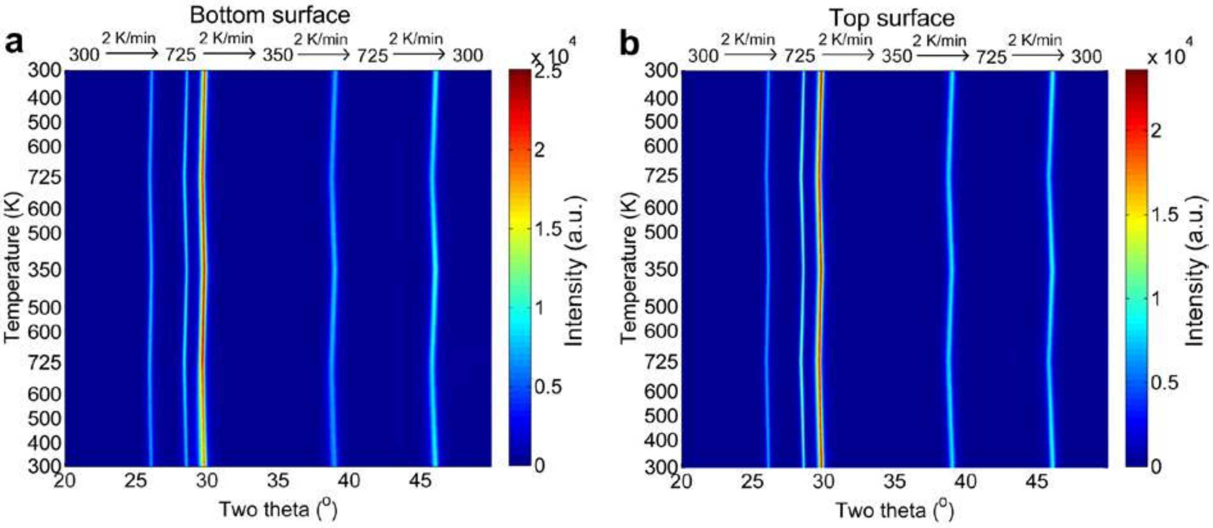

Figure 4. *In situ* XRD patterns of (a) the bottom side and (b) top side of the pellet with the composition $Mg_{3.07}Sb_{1.5}Bi_{0.48}Se_{0.02}$.

3. Electronic structure of Mg_3Sb_2 and $Mg_3Sb_{1.5}Bi_{0.5}$

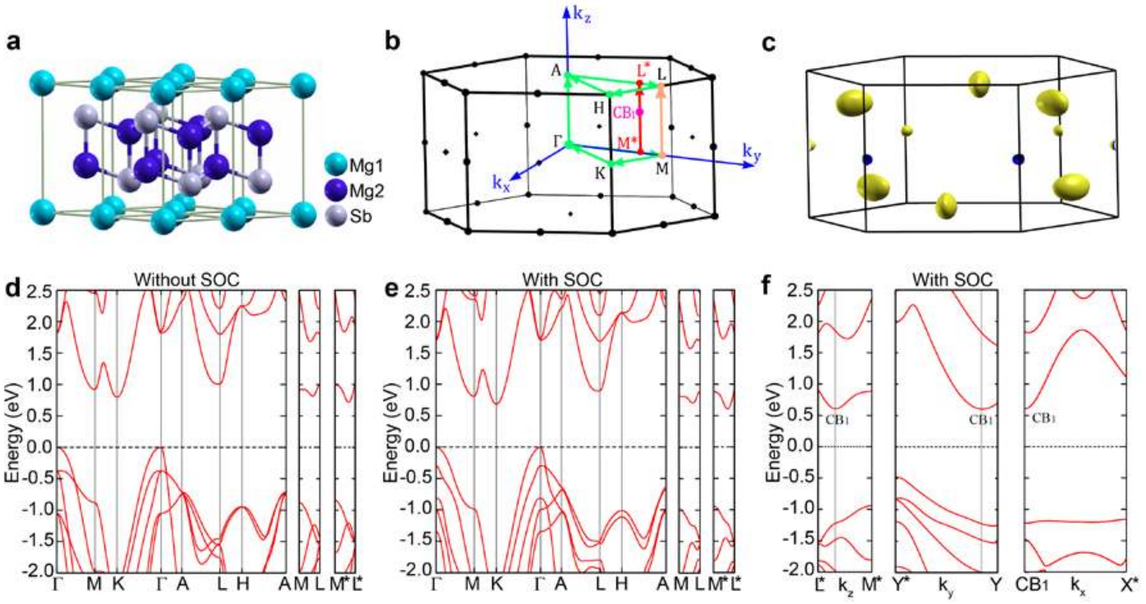

Figure 5. (a) Crystal structure, (b) high symmetry points in the first Brillouin zone, and (c) multiple carrier pockets in Fermi surface of n-type Mg_3Sb_2 corresponding to an energy level 0.02 eV above the band minimum at the K point. In (b), the location of the accurate conduction band minimum is marked as CB_1 with a coordinate of (0, 0.417, 0.333) inside the Brillouin zone. The k-path along M^* (0, 0.417, 0) and L^* (0, 0.417, 0.5) passes through CB_1. Band structures (d) without and (e) with spin orbit coupling (SOC) in Mg_3Sb_2. (f) The near-edge band structure around CB_1 along the k_x, k_y, and k_z directions. The path along the M^*-L^* line is the k_z direction. The k-path from Y^* (0, 0, 0.333) to Y (0, 0.5, 0.333) represents the k_y direction. From CB_1 to X^* (0.5, 0.417, 0.333) is along the k_x direction.

Binary Mg_3Sb_2, crystallized in La_2O_3-type structure, can be described as two dimensional Mg^{2+} layers separated by the covalently bound $[Mg_2Sb_2]^{2-}$ layers (Figure 5a).[42] The ionic Mg^{2+} layers donate electrons to the covalently bonded $[Mg_2Sb_2]^{2-}$ layers. Mg1 represents Mg atoms in the ionic Mg^{2+} layers, whereas Mg2 denotes Mg atoms in the $[Mg_2Sb_2]^{2-}$ layers. Our previous theoretical result[13] has shown that the multiple band behavior for the conduction bands results in the very promising electronic transport in n-type Mg_3Sb_2. The Fermi surface of n-type Mg_3Sb_2 is far from trivial. The typical Fermi surface of n-type Mg_3Sb_2 with an energy level 0.02 eV above the conduction band minimum at the K point elucidates the multi-valley conduction bands, i.e., six one-third electron pockets at the K point and six isolated full electron pockets close to the M-L line (see Figure 5b,c). It should be noted that the six-fold carrier pocket is actually centered in the Brillouin zone and thereby not along the M-L line. By sampling the highly dense k points homogeneously inside the Brillouin zone, we found that the center of the six-fold carrier pocket is actually located at (0, 0.417, 0.333) (Labelled CB_1), which can evolve into six equivalent positions according to the crystal symmetry (see Figure 5b). This specific k point is also where the accurate conduction band minimum (CBM) occurs. The location of CB_1 is checked to be relatively stable using a series of denser k-points and different computational methods (see Table S2, Figures S7 and S8). Surprisingly, the previous traditional band structures of Mg_3Sb_2,[13] which were calculated along the high symmetry k-paths, overlook the global minimum of conduction bands. The minimum along the M-L line is just a local minimum along some specific directions. It should be pointed out that the underlying physics behind our previous work[13] is still valid, even though the local minimum along the M-L line was used for discussion. However, it should be more accurate to use the global minimum CB_1 inside the Brillouin zone to represent the six-fold carrier pocket, which might lead to a better understanding of the electronic transport.

To elucidate the accurate CBM (CB_1), we plotted the band structure along the k-path from M^* (0, 0.417, 0) to L^* (0, 0.417, 0.5) and the result is shown in Figure 5d,e. The spin orbit coupling (SOC) results in a minor reduction in the band gap from 0.72 eV to 0.60 eV and a moderate effect on the valence bands; however, it has nearly no effect on the conduction bands. This is because the conduction bands are primarily contributed by electronic states of the light Mg atoms while the valence bands mainly come from the heavy Sb atoms.[13] Despite the negligible effect of SOC on the conduction band, we will mainly use the result with SOC for discussions. The calculation including SOC reveals that the CB_1 minimum is located at about 0.078 eV below the band minimum at the K point. By sampling the very dense k-mesh surround the CB_1 minimum, the near-edge band structure around CB_1 along the k_x, k_y, and k_z directions was calculated and shown in Figure 5f. It is clear that the band minimum CB_1 is anisotropic and the effective masses are estimated to be $m_{kx}=0.21m_e$, $m_{ky}=0.55m_e$, and $m_{kz}=0.28m_e$. The anisotropic feature of the CB_1 minimum is also expected from the ellipsoidal-like Fermi surface. Unlike CB_1, the Fermi surface of the K band minimum is roughly spherical-like with the effective mass of $m_{kx}=m_{ky}=0.32m_e$ and $m_{kz}=0.21m_e$. When the Fermi level moves 0.02 eV above the band minimum at the K point, the six full electron pockets are just tangent to the M-L lines. Moving the Fermi level further up across the local minimum along the M-L line, the M-L line will start cutting the carrier pockets (Figure S9a,b). The shape of the Fermi surface can be very sophisticated when the Fermi level cuts the local minima at the M and L points (see Figure S9c,d).

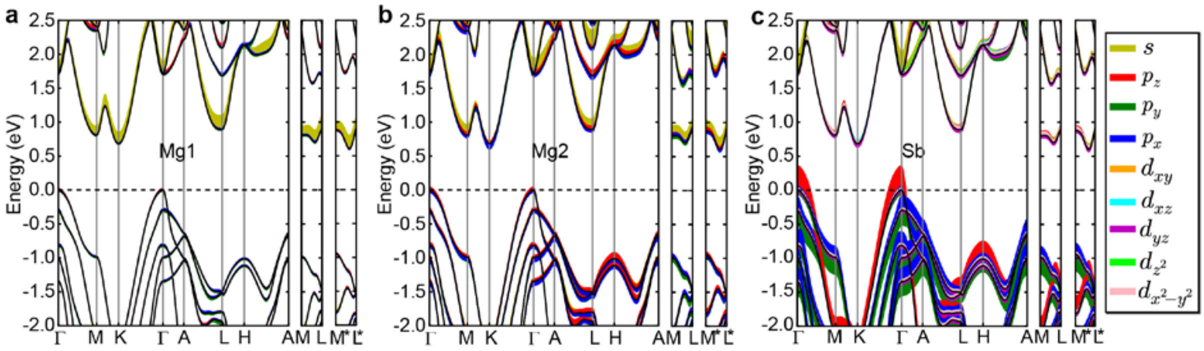

Figure 6. Orbital-projected band structures of (a) Mg1 atom, (b) Mg2 atoms, and (c) Sb atoms of Mg_3Sb_2. The band width represents the relative weight of each contribution to the band structure. The multiplicities of the Mg2 and Sb atoms were taken into account.

To obtain further insight of the underlying physics, orbital-projected band structure of Mg_3Sb_2 is simulated and shown in Figure 6. As shown in the figure, the valence bands exhibit the crystal field splitting feature between $p_{x,y}$ orbitals and p_z orbitals from Sb atoms at the Γ point. In our previous work,[8] orbital engineering approach was proposed to systematically optimize the p-type electrical transport through manipulating the relative energies of $p_{x,y}$ and p_z orbitals to achieve high orbital degeneracy. Despite the great potential of this approach, the optimization of p-type transport might be limited by the single valley degeneracy of the high symmetry Γ point. N-type transport of Mg_3Sb_2, however, is quite promising because of the complex Fermi surface induced by the multi-valley conduction bands. The CB_1 minimum along the M^*-L^* line consists mainly of *s* states from Mg1 and Mg2 atoms, which are hybridized with *p* states of Mg2 atoms and electronic states of Sb atoms. The anisotropic effective masses of the carrier pocket centered at CB_1 might be qualitatively understood by the different strengths of the overlap integrals or hybridizations along k_x, k_y, and k_z directions. The relatively heavy mass of the CB_1 minimum along Y-Y* direction is possibly caused by the weak interaction of orbitals along this specific direction. The band minimum at the K point is mainly contributed by *s* orbitals of Mg1 atom and their weak hybridizations with *p* orbitals of Mg2 atoms and *d* orbitals of Sb atoms.

Although substituting Bi on the Sb sites will not destroy the multiple band feature with band minima at the K and CB_1 points since the conduction band is mainly from the electronic states of Mg atoms, the relative energy difference and band dispersions of the two conduction minima might vary due to the changing orbital interactions. To reveal the substituting effect of Bi on the band structure, the effective band structure of $Mg_3Sb_{1.5}Bi_{0.5}$ calculated by PBE functional is shown in Figure 7a. Although PBE functional is known for its systematic underestimation of the energy gap, it usually provides the correct band dispersion, which is sufficient for this study. The result further confirms that the multiple conduction bands including band minima at the CB_1 and K points still exist in $Mg_3Sb_{1.5}Bi_{0.5}$ solid solution, consistent with our previous study. The band topologies of the CB_1 and K band minima are nearly the same as those of Mg_3Sb_2. However, compared with Mg_3Sb_2, the CB_1 minimum shifts further downward by 0.12 eV and is located at ~0.22 eV below the K minimum in $Mg_3Sb_{1.5}Bi_{0.5}$.

Figure 7. (a) Effective band structure of $Mg_3Sb_{1.5}Bi_{0.5}$ by PBE functional without SOC. (b) The energy difference $\Delta E_{\text{K-CB}_1}$ between the K band and the CB_1 band and the energy gap E_g versus the fraction x in $Mg_3Sb_{2-x}Bi_x$ solid solutions by TB-mBJ potential with SOC.

By including the correction from the CB_1 minimum, the energy difference between the band minima K and CB_1, labelled $\Delta E_{\text{K-CB}_1}$, and band gap as a function of the fraction x in $Mg_3Sb_{2-x}Bi_x$ are recalculated from our previous method (TB-mBJ potential)[13] and presented in Figure 7b. $\Delta E_{\text{K-CB}_1}$ of $Mg_3Sb_{2-x}Bi_x$ gradually increases from 0.078 eV ($x = 0$) to 0.28 eV ($x =$

2) with increasing x. The contribution of the carrier pocket at the K point to the near-edge electronic transport becomes weaker as the energy difference between CB$_1$ and K minima becomes larger. In addition, the energy gap shows a nearly linear decreasing trend from 0.6 eV ($x = 0$) to -0.02 eV ($x = 1.5$), indicating the transition from a semiconductor to a semimetal. As a result, increasing Bi content can be an effective way of promoting carrier concentration; however, the bipolar conduction effect will also become obvious due to the narrowing energy gap. Therefore, Mg$_3$Sb$_{2-x}$Bi$_x$ with $x \leq 1$ will be desirable for n-type doping. Here Mg$_3$Sb$_{1.5}$Bi$_{0.5}$ is chosen for n-type doping due to its suitable band gap of ~0.33 eV.

4. High temperature Hall data

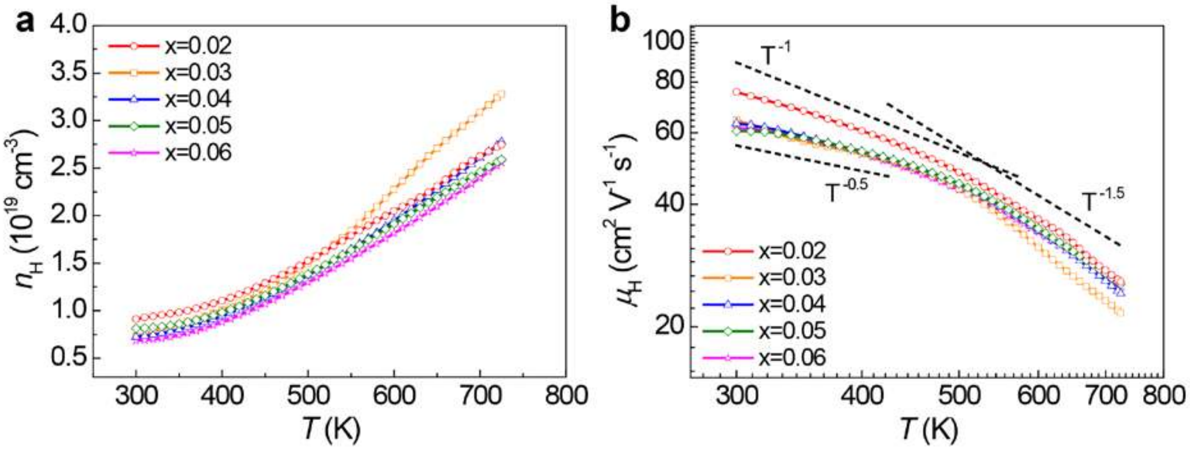

Figure 8. (a) Hall carrier concentration and (b) mobility of n-type Mg$_{3.07}$Sb$_{1.5}$Bi$_{0.5-x}$Se$_x$ samples as a function of temperature.

Hall carrier concentration, as well as its dependence on temperature, was measured and shown in Figure 8a. Se-doped samples show a narrow distribution of the room-temperature electron concentration from 6.85 × 10^{18} cm^{-3} to 9.10 × 10^{18} cm^{-3}, which is slightly lower than the previously reported Te-doped samples.[13] For all Se-doped samples, the Hall carrier concentration curves clearly exhibit two regions: first weak temperature dependence below 400 K and then a nearly linear increasing trend with rising temperature due to the activation of intrinsic carriers. At room temperature, the sample with $x = 0.02$ shows the highest carrier concentration of 9.10×10^{18} cm^{-3}, which then increases to 2.75×10^{19} cm^{-3} at 725 K.

As shown in Figure 8b, the mobility shows a decreasing trend as the temperature increases, and roughly follows the temperature dependence of T^{-p} $(1 \leq p \leq 1.5)$. This indicates the acoustic phonon scattering mechanism is dominant. Between 300-400 K, the temperature dependence deviates from the T^{-1} relation and approaches $T^{-0.5}$, suggesting the contribution from the alloy scattering.[43] The room-temperature mobility values of Se-doped samples are within the range of 61.6-75.6 cm^2 V^{-1} s^{-1}, which are comparable to the reported Te-doped ones,[13] but by a factor of at least 3.8 larger than that of the pure Mg_3Sb_2 (μ = 16 cm^2 V^{-1} s^{-1} at n_H = 1.3×10^{19} cm^{-3}).[21] The large enhancement of mobility in n-type Se-doped $Mg_3Sb_{1.5}Bi_{0.5}$ reveals the light effective mass of the CB_1 minimum with six conducting carrier pockets suggested by theory. Among all samples, $Mg_{3.07}Sb_{1.5}Bi_{0.48}Se_{0.02}$ shows the highest mobility from 75.6 cm^2 V^{-1} s^{-1} at 300 K to 25.8 cm^2 V^{-1} s^{-1} at 725 K.

5. Electronic transport modelling

The electrical transport property of a material often shows a strong dependence on the degeneracy and topology of the near-edge electronic bands. The Seebeck coefficient can be determined by the density of states effective mass $m^* = N_v^{2/3} m_s^*$, where N_v denotes the valley degeneracy of the electronic bands and m_s^* represents the effective mass of a single valley.[2,44] Moreover, for a semiconductor with multi-valley electronic bands, the optimum electrical transport performance can be expressed as being proportional to the weighted mobility $\mu(m_d^*/m_e)^{3/2}$, where μ and m_e represent the carrier mobility and the mass of an electron, respectively.[2,5,11] Considering the predominant acoustic phonon scattering or alloy scattering in this work, the carrier mobility is expected to be $\mu \propto 1/(m_I^* m_s^{*3/2})$, where m_I^* is the conductivity effective mass. Eventually, the weighted mobility can be simplified and written as N_v/m_I^* (N_v/m_s^* for an isotropic band). It is clear that the excellent electrical performance requires a high valley degeneracy as well as a light conductivity effective mass. Thus, the CB_1 band minimum with a high valley degeneracy of 6 and a relatively low $m_I^* = 0.30m_e$ is highly conducive to the electrical transport in n-type Mg_3Sb_2-based compounds. Since the CBM is occupied by the CB_1 minimum in Mg_3Sb_2 and $Mg_3Sb_{1.5}Bi_{0.5}$, the CB_1 band minimum thereby makes the dominant contribution to the n-type electrical transport. In contrast, the valence band maximum located at the Γ point only has one single valley degeneracy and a slightly heavier m_I^*=0.36m_e. This is why Seebeck coefficient and power factor of n-type doping in Mg_3Sb_2 predicted by integrated *ab initio* full band structure and semi-classical Boltzmann transport theory are much better than those of p-type doping (Figure 9).

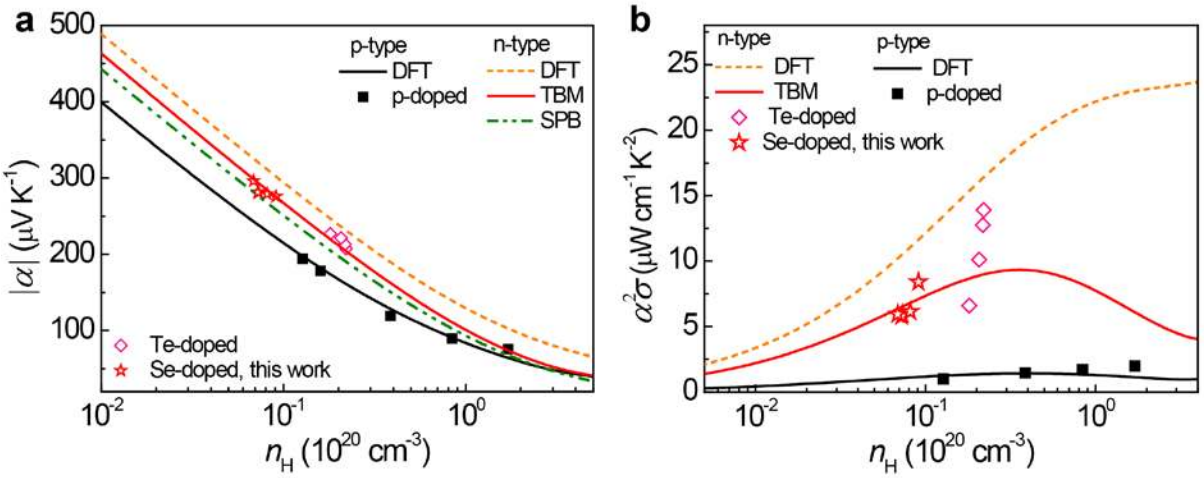

Figure 9. (a) The absolute value of Seebeck coefficient ($|\alpha|$) and (b) power factor as a function of Hall carrier concentration at room temperature. In (a) and (b), the black solid and orange dashed lines represent the predictions of p-type and n-type Mg_3Sb_2 by full DFT band structure calculation from our previous work.[13] The red solid line represents the result from a three band model (TBM) for n-type $Mg_3Sb_{1.5}Bi_{0.5}$.

The Green dashed line shows the expected $|\alpha|$ versus n_{H} behavior for a single parabolic band (SPB) with the effective mass equal to the individual conduction band minimum CB_1 along the M^*-L^* line at the band edges.[13] The black solid points are the reported p-type doped Mg_3Sb_2 from the refs. 19-21. The pink diamonds represent the previously reported n-type Te-doped $Mg_3Sb_{1.5}Bi_{0.5}$.[13] The red stars are Se-doped $Mg_{3.07}Sb_{1.5}Bi_{0.5}$ samples from this work.

Additionally, the Seebeck coefficient modeled by a single band with the effective mass of the CB_1 band minimum and acoustic phonon scattering is lower than that predicted by full band structure calculation (Figure 9a), indicating the contribution from the secondary band minimum K. The energy difference between the CB_1 and K minimum is around 0.078 eV, which is a small value comparable to ~$3k_B T$ at room temperature. The two band minima can even be considered as effectively converged at elevated temperatures due to the broadening of Fermi integral. This reveals that the contribution from the K band minimum should not be overlooked in n-type Mg_3Sb_2. However, in $Mg_3Sb_{1.5}Bi_{0.5}$ the band minimum at the K point is located at 0.22 eV above CB_1, which is around 3 times larger than that of Mg_3Sb_2. Hence, compared with Mg_3Sb_2, the contribution of the band minimum K to the electrical transport is definitely weak in $Mg_3Sb_{1.5}Bi_{0.5}$. This explains the lower experimental values for Seebeck coefficient and power factor in n-type doped $Mg_3Sb_{1.5}Bi_{0.5}$ with respect to those predicted by DFT for n-type Mg_3Sb_2 (Figure 9).

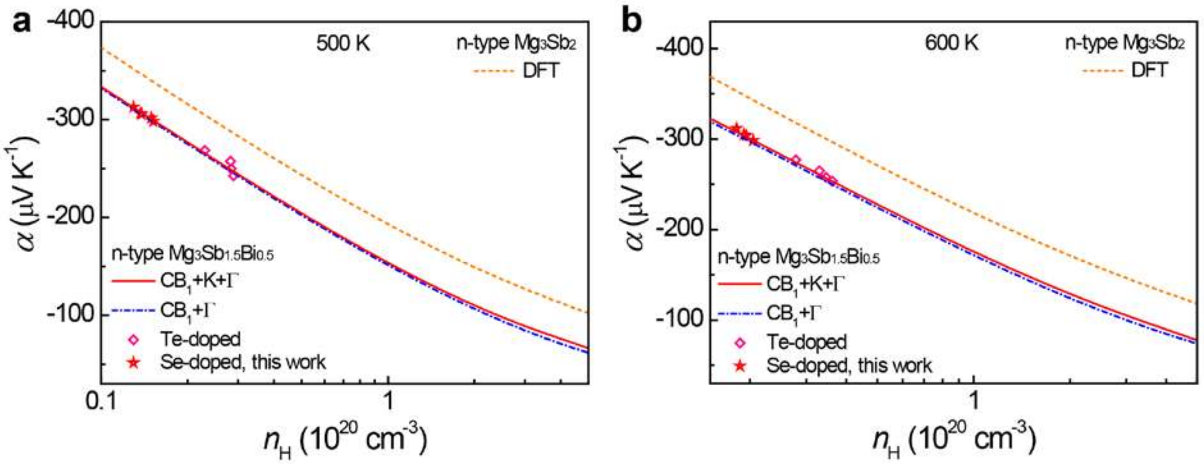

Figure 10. The Seebeck coefficient at (a) 500 K and (b) 600 K versus Hall carrier concentration. The orange dashed lines represent the predictions of n-type Mg_3Sb_2 by full DFT band structure calculation. The pink diamonds represent the previously reported n-type Te-doped $Mg_3Sb_{1.5}Bi_{0.5}$.[13] The red stars are Se-doped $Mg_{3.07}Sb_{1.5}Bi_{0.5}$ samples from this work. The red solid lines and the dashed blue lines represent the predictions from a three band model including the near-edge conduction bands at the CB_1, K, and Γ points (CB_1+K+Γ) and a two band model considering the band minima CB_1 and Γ (CB_1+Γ), respectively.

In order to have a better understanding of the electrical transport in n-type $Mg_3Sb_{1.5}Bi_{0.5}$, a three band model (TBM), including the contributions from the near-edge conduction bands at the CB_1 and K points and the valence band at the Γ point, was used for the further analysis. Including the valence band maximum at the Γ point into the modelling is important since the bipolar contributions might affect the electrical transport at elevated temperatures due to the small band gap of 0.33 eV in $Mg_3Sb_{1.5}Bi_{0.5}$. For the details of this model, please refer to Supporting Information. All transport properties were calculated according to the formula for a multi-band system suggested by Putley.[40] Instead of fitting the experimental data, most of the input parameters were taken from *ab initio* calculation (Table S3). Although the alloy scattering is dominant at room temperature, the carrier scattering by acoustic phonons starts playing a crucial role with increasing temperature (Figure 8b). Furthermore, $Mg_3Sb_{1.5}Bi_{0.5}$ is a polar semiconductor with relatively strong polar covalent bonding[45] and thereby might show strong polar optical scattering.[46,47] Including the polar optical scattering might be important for the understanding of the electrical transport in n-type $Mg_3Sb_{1.5}Bi_{0.5}$. Therefore, here the alloy scattering, the acoustic phonon scattering, and the polar optical scattering are all taken into consideration in the model. The total carrier's scattering time τ can then be deduced by Matthiessen's rule:

$$\frac{1}{\tau}=\frac{1}{\tau_{\mathrm{ac}}}+\frac{1}{\tau_{\mathrm{al}}}+\frac{1}{\tau_{\mathrm{po}}}, \tag{1}$$

where τ_{ac}, τ_{al}, and τ_{po} are the carrier's scattering time corresponding to the acoustic phonon, alloy, and polar optical scattering. With the total carrier's scattering time, the electrical transport properties can be quantitatively derived (see Supporting Information for details).

The results from the three band model are shown in Figures 9, S10, and 10. It is obvious that the simulation by the three band model agrees quite well with the experimental data including the previously reported n-type Te-doped $Mg_3Sb_{1.5}Bi_{0.5}$ (ref. 13) and Se-doped $Mg_{3.07}Sb_{1.5}Bi_{0.5}$ from this work. In order to analyze the contribution of the band minimum at the K point to the electrical transport, the predictions based on a two band model considering the conduction band at the CB_1 point and the valence band at the Γ point are also plotted in Figures S10 and 10 for comparison. At low temperatures, the Seebeck coefficient curve predicted by the two band model is nearly the same as that simulated by the three band model at the carrier concentration below 10^{20} cm^{-3}. The experimental data all show relatively low carrier concentrations below 10^{20} cm^{-3}. In general, the contribution from the band minimum at the K point is gradually increasing with rising temperature. However, even at elevated temperatures (such as 500 K and 600 K), the result from the three band model is just slightly higher than that from the two band model, indicating the relatively weak contribution from the K band minimum in n-type $Mg_3Sb_{1.5}Bi_{0.5}$. This again confirms the theoretical result that the K band minimum occurs at 0.22 eV above CB_1 in n-type $Mg_3Sb_{1.5}Bi_{0.5}$, which is much larger than that in n-type Mg_3Sb_2. Compared with n-type $Mg_3Sb_{1.5}Bi_{0.5}$, the nearly effective convergence of the K and CB_1 band minima in n-type Mg_3Sb_2 at elevated temperatures maximizes the contribution from the secondary K band minimum and thus leads to the much higher Seebeck values predicted by DFT (Figure 10). Therefore, further optimization of the electrical transport performance in n-type Mg_3Sb_2-based compounds will be expected if the energy difference between the CB_1 and K minima can be minimized or the effect of the K band minimum can be maximized by tuning the suitable n-type dopants.

6. High temperature transport properties

Figure 11 depicts the temperature dependences of thermoelectric transport properties of $Mg_{3.07}Sb_{1.5}Bi_{0.5-x}Se_x$ (x = 0.02-0.06). For the samples with x = 0.03-0.06, the resistivity curves show three regions: firstly, a slowly decreasing trend from 300 K to ~360 K; then, a relatively fast drop with thermally activated semiconducting behavior to ~600K; finally, a nearly temperature independent or very slow increasing trend up to 725 K (Figure 11a). Unlike these samples, the resistivity of the sample with x = 0.02 shows a low value of 9.068 mΩ cm at room temperature, which slowly increases to a maximum of 9.409 mΩ cm at 370 K, then decreases to a minimum of 8.293 mΩ cm at 590 K, and finally increases to 8.818 mΩ cm at 725 K. For all samples (except x = 0.05), the resistivity follows a systematic increasing tendency with increasing Se content. The exception might be attributed to the effect of the secondary phase in this particular sample. Similarly, the Seebeck coefficients of Se-doped $Mg_{3.07}Sb_{1.5}Bi_{0.5}$ also possess three regions with slightly different temperature transition points (Figure 11b). Room-temperature Seebeck coefficient values of the Se-doped samples are distributed in the range from 275.9 μV K^{-1} to 296.3 μV K^{-1}, which are higher than those of the reported Te-doped samples.[13] This result is expected from the lower carrier concentration in Se-doped samples. In general, the absolute values of Seebeck coefficients increase with increasing Se content. Consequently, the sample with $x = 0.02$ has the lowest Seebeck value of 275.9 μV K^{-1} at room temperature, which reaches a local maximum of 300 μV K^{-1} at 550 K, and then slightly decreases at 550-625 K followed by a gentle increase to 304 μV K^{-1} at 725 K.

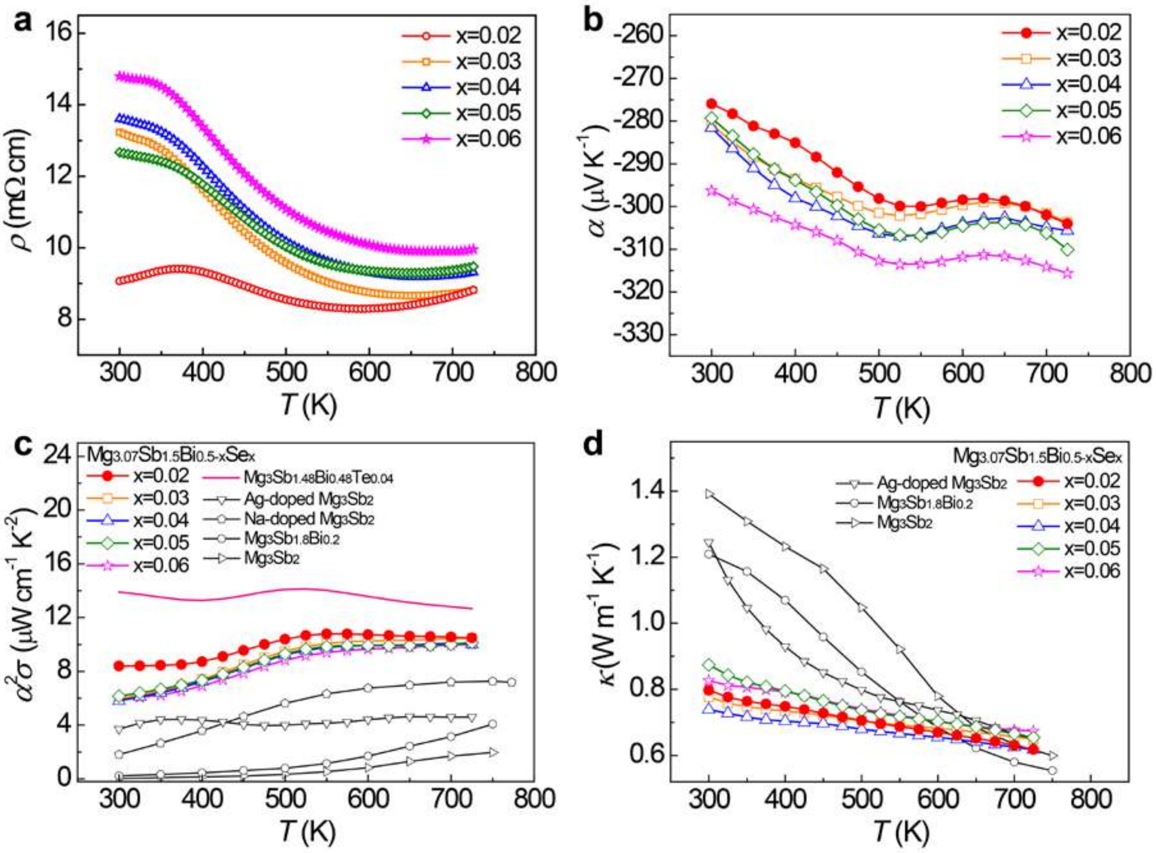

Figure 11. Temperature dependence of (a) electrical resistivity, (b) Seebeck coefficient, (c) power factor, and (d) total thermal conductivity of n-type $Mg_{3.07}Sb_{1.5}Bi_{0.5-x}Se_x$. In (c) and (d), the reported data of n-type $Mg_3Sb_{1.48}Bi_{0.48}Te_{0.04}$,[13] p-type Mg_3Sb_2,[22] $Mg_3Sb_{1.8}Bi_{0.2}$,[22] Ag-doped Mg_3Sb_2,[20] and Na-doped Mg_3Sb_2 (ref. 19) are plotted for comparison.

As shown in Figure 11c, the $Mg_{3.07}Sb_{1.5}Bi_{0.48}Se_{0.02}$ sample exhibits the highest power factor within the whole temperature range. At low temperatures, the power factor of $Mg_{3.07}Sb_{1.5}Bi_{0.48}Se_{0.02}$ is much better than the other Se-doped samples due to the significantly lower resistivity. However, the power factors of all samples are comparable in the high temperature range of 650-725 K. The power factor of the sample with $x = 0.02$ at room temperature is 8.39 $\mu W\ cm^{-1}\ K^{-2}$, which reaches a peak value of 10.79 $\mu W\ cm^{-1}\ K^{-2}$ at 550 K and then decreases to 10.49 $\mu W\ cm^{-1}\ K^{-2}$ at 725 K. The room-temperature power factor of the best Se-doped sample here are much lower than that of the reported Te-doped sample (13.9 $\mu W\ cm^{-1}\ K^{-2}$).[13] However, the power factors of the Se-doped samples are considerably higher than those of p-type Mg_3Sb_2-based compounds, e.g., Mg_3Sb_2,[22] Na-doped Mg_3Sb_2,[19] Ag-doped Mg_3Sb_2,[20] and $Mg_3Sb_{1.8}Bi_{0.2}$.[22]

The total thermal conductivity values of $Mg_{3.07}Sb_{1.5}Bi_{0.5-x}Se_x$ ($x = 0.02$-0.06) and their dependencies on temperature are presented in Figure 11d. The total thermal conductivity of each sample displays a decreasing trend with increasing temperature. The sample with $x = 0.04$ shows the lowest κ of 0.739-0.617 $W\ m^{-1}\ K^{-1}$ within the entire temperature range of 300-725 K. Thermal conductivity of $Mg_{3.07}Sb_{1.5}Bi_{0.48}Se_{0.02}$, the one with the highest power factor, has a slightly high value of 0.797 $W\ m^{-1}\ K^{-1}$ at room temperature and then reduces to a value of 0.618 $W\ m^{-1}\ K^{-1}$ at 725 K, which is comparable to the lowest value in all samples. In comparison with p-type Mg_3Sb_2,[22] $Mg_3Sb_{1.8}Bi_{0.2}$,[22] and Ag-doped Mg_3Sb_2,[20] the n-type Se-doped samples show much lower thermal conductivity values at low temperatures, which might be explained by alloy scattering or point defect scattering of phonons. This implies that the low thermal conductivity will certainly contribute to the overall performance at low temperatures. However, the high-temperature thermal conductivities of n-type Se-doped samples are comparable to those of p-type compounds, indicating that the excellent power factor is the main origin of the high thermoelectric performance at high temperatures.

7. Lattice thermal conductivity

The total thermal conductivity is the sum of the contributions from three components, i.e., the lattice thermal conductivity κ_L, the electron thermal conductivity κ_e, and the bipolar thermal conductivity κ_{bip}. κ_e can be estimated by the Wiedemann-Franz law $\kappa_e = L\sigma T$, where the total Lorenz number L shown in Figure S11 is calculated from the conductivity weighted average over L of each band based on a three band model:[40]

$$L = (L_{CB_1}\sigma_{CB_1} + L_K\sigma_K + L_\Gamma\sigma_\Gamma) / (\sigma_{CB_1} + \sigma_K + \sigma_\Gamma)\,, \tag{2}$$

the subscripts CB_1, K, and Γ represent the contributions from the corresponding electronic bands. According to the multiband model proposed by Putley,[40] κ_{bip} is the product of the difference between the sum of the power factors of the individual bands and the total power factor, and can be calculated by:[40]

$$\kappa_{bip} = T\left[\sum_{i=CB_1,K,\Gamma} \alpha_i^2\sigma_i - \left(\sum_{i=CB_1,K,\Gamma} \alpha_i\sigma_i\right)^2 \Bigg/ \sum_{i=CB_1,K,\Gamma} \sigma_i\right]. \tag{3}$$

For narrow gap semiconductors, the bipolar effect on the thermal conductivity can be very important at elevated temperatures due to the existence of both electrons and holes. κ_{bip} of

Se-doped samples displays a rapidly increasing trend at high temperatures (Figure 12a), and shows a maximum value of ~0.05 W m^{-1} K^{-1} at 725 K, which is less than 9% of the total thermal conductivity. This reveals the relatively small contribution of the bipolar effect to the thermal conductivity in Se-doped samples.

By subtracting κ_e and κ_{bip} from the total thermal conductivity, the lattice thermal conductivity data of all Se-doped samples (κ_L) are obtained and shown in Figure 12b. It is clear that the lattice component is the main contribution to the total thermal conductivity. The temperature dependence of κ_L for all samples roughly follows $T^{-0.5}$ relation in the temperature range of 300-625 K, which is probably induced by the dominant point defect scattering.[48] At high temperatures above 625 K, the temperature-dependent κ_L approaches T^{-1} relation, suggesting Umklapp scattering of acoustic phonons to be dominant with increasing temperature.[49]

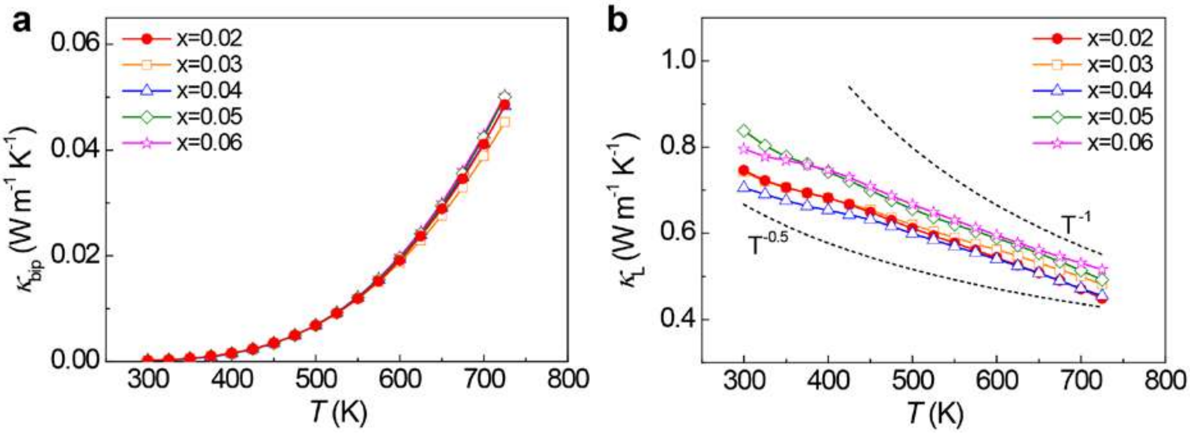

Figure 12. (a) The bipolar thermal conductivity and (b) the lattice thermal conductivity as a function of temperature in n-type $Mg_{3.07}Sb_{1.5}Bi_{0.5-x}Se_x$ (x = 0.02-0.06).

8. Dimensionless figure of merit

The dimensionless *zT* as a function of temperature is shown in Figure 13a. Among all samples, the $Mg_{3.07}Sb_{1.5}Bi_{0.48}Se_{0.02}$ sample shows the best performance with a room-temperature *zT* of 0.32, which increases to an optimum value of 1.23 at 725 K. Compared with the pristine Mg_3Sb_2,[22] all Se-doped samples show strongly enhanced *zT* within the entire temperature region (Figure 13b). In addition, the thermoelectric *zT* of the n-type Se-doped sample with $x = 0.02$ is at least 2 times higher than that of p-type Mg_3Sb_2-based compounds including $Mg_3Sb_{1.8}Bi_{0.2}$,[22] Ag-doped Mg_3Sb_2,[20] and Na-doped Mg_3Sb_2.[19] The high thermoelectric performance at low temperatures can be attributed to the reduction in thermal conductivity as well as the improved electrical performance, while at high temperatures it mainly originates from the considerably enhanced power factor. The good electrical transport properties can be well explained by the multiple band behavior dominated by a nontrivial conduction band with six-fold valley degeneracy. In comparison with the reported Te-doped $Mg_3Sb_{1.5}Bi_{0.5}$,[13] the performance of the Se-doped samples is slightly lower due to their lower carrier concentrations (Figure 13b). The better performance of Te doping over Se doping on Sb sites has also been observed in the recently discovered CoSbS.[50,51] However, we can expect a further improvement of *zT* through increasing the carrier concentration via co-doping or slightly adjusting Bi content.

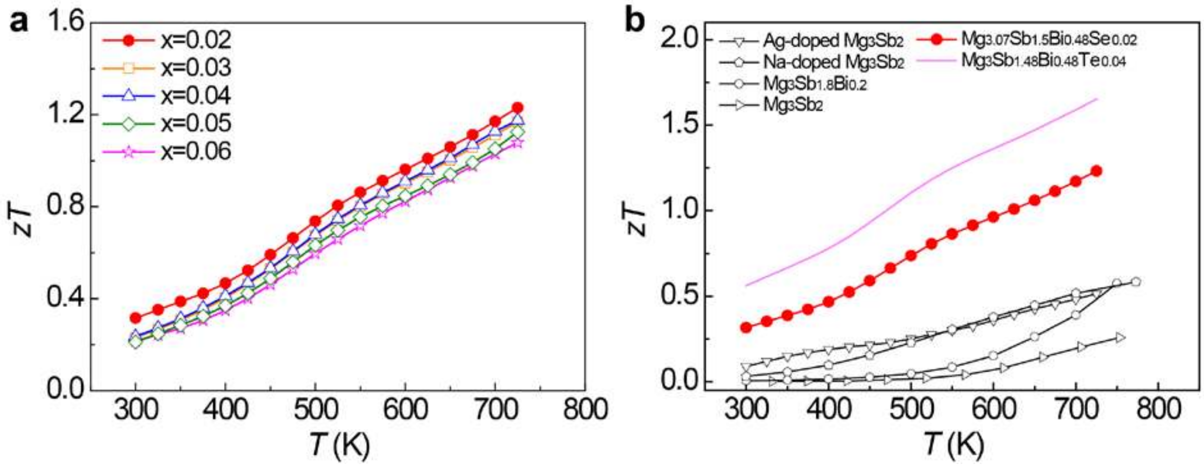

Figure 13. (a) The dimensionless figure of merit (zT) as a function of temperature for n-type $Mg_{3.07}Sb_{1.5}Bi_{0.5\text{-}x}Se_x$. (b) zT in n-type $Mg_{3.07}Sb_{1.5}Bi_{0.48}Se_{0.02}$ and the comparison with the reported n-type $Mg_3Sb_{1.48}Bi_{0.48}Te_{0.04}$,[13] p-type Ag-doped Mg_3Sb_2,[20] Mg_3Sb_2,[19] $Mg_3Sb_{1.8}Bi_{0.2}$,[22] and Mg_3Sb_2.[22]

CONCLUSION

In summary, we present a new low-cost Te-free thermoelectric material, n-type $Mg_{3.07}Sb_{1.5}Bi_{0.5\text{-}x}Se_x$, with a high figure of merit of 1.23 at 725 K. In comparison with pure Mg_3Sb_2 and other p-type doped Mg_3Sb_2, the considerably enhanced zT at low temperatures is caused by the simultaneous improvements in the power factor and thermal conductivity, whereas the high temperature zT is mainly contributed by the superior power factor. The low thermal conductivity is possibly induced by the enhanced point defect scattering for phonons, while the excellent electrical transport performance can be attributed to a unique conduction band with a light conductivity effective mass and a high valley degeneracy of 6. The systematic study on the electronic structure of n-type $Mg_3Sb_{1.5}Bi_{0.5}$ reveals the actual location of the conduction band minimum and its relatively large energy separation (~0.22 eV) from the secondary conduction band minimum. The theoretical result confirms the weak contribution of the secondary conduction band minimum to the electrical transport in n-type

$Mg_3Sb_{1.5}Bi_{0.5}$. Considering the earth-abundant and inexpensive component elements, n-type Se-doped $Mg_3Sb_{1.5}Bi_{0.5}$ shows great potential for the medium-temperature thermoelectric application.

ASSOCIATED CONTENT

Supporting Information:

Temperature dependence of resistivity with both heating and cooling curves for different cycles; Seebeck coefficients measured during heating; *zT* of the high performance pellet x=0.02 for different cycles; temperature dependence of thermal diffusivity and heat capacity; band structures of Mg_3Sb_2 by PBE functional without and with spin orbit coupling; band structure of Mg_3Bi_2 by mBJ potential with spin orbit coupling; Fermi surfaces of n-type Mg_3Sb_2 corresponding to several different energy levels; Seebeck coefficient at 300 K and 400 K as a function of Hall carrier concentration; the Lorenz number calculated by a three band model; the sample density measured by Archimedes method; the location of the accurate conduction band minimum CB_1 with a series of denser k-points and different methods; physical properties of $Mg_3Sb_{1.5}Bi_{0.5}$ that used for the electronic transport modelling; a short description of electrical transport properties; the calculation details of the three band model.

AUTHOR INFORMATION

Corresponding Author

B.B.I. (bo@chem.au.dk).

Notes:
The authors declare no competing financial interests.

ACKNOWLEDGMENT

This work was supported by the Danish National Research Foundation (DNRF93) and the Danish Center for Scientific Computing. The authors thank K. F. F. Fischer and H. Reardon for comments.

REFERENCES

(1) Snyder, G. J.; Toberer, E. S. Complex thermoelectric materials. *Nat. Mater.* **2008**, *7*, 105-114.

(2) Nolas, G. S.; Sharp, J.; Goldsmid, H. J. *Thermoelectrics: Basic Principles and New Materials Developments*; Springer, New York, 2001.

(3) Biswas, K.; He, J.; Blum, I. D.; Wu, C.-I.; Hogan, T. P.; Seidman, D. N.; Dravid, V. P.; Kanatzidis, M. G. High-performance bulk thermoelectrics with all-scale hierarchical architectures. *Nature* **2012**, *489*, 414-418.

(4) Heremans, J. P.; Jovovic, V.; Toberer, E. S.; Saramat, A.; Kurosaki, K.; Charoenphakdee, A.; Yamanaka, S.; Snyder, G. J. Enhancement of thermoelectric efficiency in PbTe by distortion of the electronic density of states. *Science* **2008**, *321*, 554-557.

(5) Pei, Y.; Shi, X.; LaLonde, A.; Wang, H.; Chen, L.; Snyder, G. J. Convergence of electronic bands for high performance bulk thermoelectrics. *Nature* **2011**, *473*, 66-69.

(6) Snyder, G. J.; Christensen, M.; Nishibori, E.; Caillat, T.; Iversen, B. B. Disordered zinc in Zn_4Sb_3 with phonon-glass and electron-crystal thermoelectric properties. *Nat. Mater.* **2004**, *3*, 458-463.

(7) Hsu, K. F.; Loo, S.; Guo, F.; Chen, W.; Dyck, J. S.; Uher, C.; Hogan, T.; Polychroniadis, E. K.; Kanatzidis, M. G. Cubic $AgPb_mSbTe_{2+m}$: Bulk thermoelectric materials with high figure of merit. *Science* **2004**, *303*, 818-821.

(8) Zhang, J.; Song, L.; Madsen, G. K. H.; Fischer, K. F. F.; Zhang, W.; Shi, X.; Iversen, B. B. Designing high-performance layered thermoelectric materials through orbital engineering. *Nat. Commun.* **2016**, *7*, 10892.

(9) Liu, H. L.; Shi, X.; Xu, F. F.; Zhang, L. L.; Zhang, W. Q.; Chen, L. D.; Li, Q.; Uher, C.; Day, T.; Snyder, G. J. Copper ion liquid-like thermoelectrics. *Nat. Mater.* **2012**, *11*, 422-425.

(10) Zaitsev, V. K.; Fedorov, M. I.; Gurieva, E. A.; Eremin, I. S.; Konstantinov, P. P.; Samunin, A. Y.; Vedernikov, M. V. Highly effective $Mg_2Si_{1-x}Sn_x$ thermoelectrics. *Phys. Rev. B* **2006**, *74*, 045207.

(11) Zhang, J.; Liu, R.; Cheng, N.; Zhang, Y.; Yang, J.; Uher, C.; Shi, X.; Chen, L.; Zhang, W. High-performance pseudocubic thermoelectric materials from non-cubic chalcopyrite compounds. *Adv. Mater.* **2014**, *26*, 3848-3853.

(12) Bhattacharya, S.; Madsen, G. K. H. High-throughput exploration of alloying as design strategy for thermoelectrics. *Phys. Rev. B* **2015**, *92*, 085205.

(13) Zhang, J.; Song, L.; Pedersen, S. H.; Yin, H.; Hung, L. T.; Iversen, B. B. Discovery of high-performance low-cost n-type Mg_3Sb_2-based thermoelectric materials with multi-valley conduction bands. *Nat. Commun.* **2017**, *8*, 13901.

(14) Xie, H.; Wang, H.; Pei, Y.; Fu, C.; Liu, X.; Snyder, G. J.; Zhao, X.; Zhu, T. Beneficial contribution of alloy disorder to electron and phonon transport in half-heusler thermoelectric materials. *Adv. Funct. Mater.* **2013**, *23*, 5123-5130.

(15) Christensen, M.; Abrahamsen, A. B.; Christensen, N. B.; Juranyi, F.; Andersen, N. H.; Lefmann, K.; Andreasson, J.; Bahl, C. R. H.; Iversen, B. B. Avoided crossing of rattler modes in thermoelectric materials. *Nat. Mater.* **2008**, *7*, 811-815.

(16) Condron, C. L.; Kauzlarich, S. M.; Gascoin, F.; Snyder, G. J. Thermoelectric

properties and microstructure of Mg_3Sb_2. *J. Solid State Chem.* **2006**, *179*, 2252-2257.

(17) Kim, S.; Kim, C.; Hong, Y.-K.; Onimaru, T.; Suekuni, K.; Takabatake, T.; Jung, M.-H. Thermoelectric properties of Mn-doped Mg-Sb single crystals. *J. Mater. Chem. A* **2014**, *2*, 12311-12316.

(18) Bhardwaj, A.; Misra, D. K. Enhancing thermoelectric properties of a p-type Mg_3Sb_2-based Zintl phase compound by Pb substitution in the anionic framework. *RSC Adv.* **2014**, *4*, 34552-34560.

(19) Shuai, J.; Wang, Y.; Kim, H. S.; Liu, Z.; Sun, J.; Chen, S.; Sui, J.; Ren, Z. Thermoelectric properties of Na-doped Zintl compound: $Mg_{3-x}Na_xSb_2$. *Acta Mater.* **2015**, *93*, 187-193.

(20) Song, L.; Zhang, J.; Iversen, B. B. Simultaneous improvement of power factor and thermal conductivity via Ag doping in p-type Mg_3Sb_2 thermoelectric materials. *J. Mater. Chem. A* **2017,** *5*, 4932-4939

(21) Ponnambalam, V.; Morelli, D. T. On the Thermoelectric properties of Zintl compounds $Mg_3Bi_{2-x}Pn_x$ (Pn = P and Sb). *J. Electron. Mater.* **2013**, *42*, 1307-1312.

(22) Bhardwaj, A.; Rajput, A.; Shukla, A. K.; Pulikkotil, J. J.; Srivastava, A. K.; Dhar, A.; Gupta, G.; Auluck, S.; Misra, D. K.; Budhani, R. C. Mg_3Sb_2-based Zintl compound: a non-toxic, inexpensive and abundant thermoelectric material for power generation. *RSC Adv.* **2013**, *3*, 8504-8516.

(23) Tamaki, H.; Sato, H. K.; Kanno, T. Isotropic conduction network and defect chemistry in $Mg_{3+\delta}Sb_2$-based layered Zintl compounds with high thermoelectric performance. *Adv. Mater.* **2016**, *28*, 10182-10187.

(24) Shuai, J.; Mao, J.; Song, S.; Zhu, Q.; Sun, J.; Wang, Y.; He, R.; Zhou, J.; Chen, G.; Singh, D. J.; Ren, Z. Tuning the carrier scattering mechanism to effectively improve the thermoelectric properties. *Energy Environ. Sci.* **2017**, *10*, 799-807.

(25) Hu, Z.; Gao, S. Upper crustal abundances of trace elements: A revision and update. *Chem. Geol.* **2008**, *253*, 205-221.

(26) LeBlanc, S.; Yee, S. K.; Scullin, M. L.; Dames, C.; Goodson, K. E. Material and manufacturing cost considerations for thermoelectrics. *Renew. Sustainable Energy Rev.* **2014**, *32*, 313-327.

(27) Rodríguez-Carvajal, J. Recent advances in magnetic structure determination by neutron powder diffraction. *Physica B* **1993**, *192*, 55-69.

(28) Borup, K. A.; Toberer, E. S.; Zoltan, L. D.; Nakatsukasa, G.; Errico, M.; Fleurial, J.-P.; Iversen, B. B.; Snyder, G. J. Measurement of the electrical resistivity and Hall coefficient at high temperatures. *Rev. Sci. Instrum.* **2012**, *83*, 123902.

(29) Borup, K. A.; de Boor, J.; Wang, H.; Drymiotis, F.; Gascoin, F.; Shi, X.; Chen, L.; Fedorov, M. I.; Muller, E.; Iversen, B. B.; Snyder, G. J. Measuring thermoelectric transport properties of materials. *Energy Environ. Sci.* **2015**, *8*, 423-435.

(30) Iwanaga, S.; Toberer, E. S.; LaLonde, A.; Snyder, G. J. A high temperature apparatus for measurement of the Seebeck coefficient. *Rev. Sci. Instrum.* **2011**, *82*, 063905.

(31) Blaha, P.; Schwarz, K.; Madsen, G. K. H.; Kvasnicka, D.; Luitz, J. *An Augmented Plane Wave and Local Orbitals Program for Calculating Crystal Properties* (Technical University of Wien, Vienna, 2001).

(32) Tran, F.; Blaha, P. Accurate band gaps of semiconductors and insulators with a

semilocal exchange-correlation potential. *Phys. Rev. Lett.* **2009**, *102*, 226401.

(33) Zhang, Y.; Zhang, J.; Gao, W.; Abtew, T. A.; Wang, Y.; Zhang, P.; Zhang, W. Near-edge band structures and band gaps of Cu-based semiconductors predicted by the modified Becke-Johnson potential plus an on-site Coulomb U. *J. Chem. Phys.* **2013**, *139*, 184706.

(34) Perdew, J. P.; Burke, K.; Ernzerhof, M. Generalized gradient approximation made simple. *Phys. Rev. Lett.* **1996**, *77*, 3865-3868.

(35) Kokalj, A. Computer graphics and graphical user interfaces as tools in simulations of matter at the atomic scale. *Comput. Mater. Sci.* **2003**, *28*, 155-168.

(36) Kresse, G.; Furthmüller, J. Efficient iterative schemes for ab initio total-energy calculations using a plane-wave basis set. *Phys. Rev. B* **1996**, *54*, 11169-11186.

(37) Medeiros, P. V. C.; Stafström, S.; Björk, J. Effects of extrinsic and intrinsic perturbations on the electronic structure of graphene: Retaining an effective primitive cell band structure by band unfolding. *Phys. Rev. B* **2014**, *89*, 041407.

(38) Medeiros, P. V. C.; Tsirkin, S. S.; Stafström, S.; Björk, J. Unfolding spinor wave functions and expectation values of general operators: Introducing the unfolding-density operator. *Phys. Rev. B* **2015**, *91*, 041116.

(39) Madsen, G. K. H.; Singh, D. J. BoltzTraP. A code for calculating band-structure dependent quantities. *Comput. Phys. Commun.* **2006**, *175*, 67-71.

(40) Putley, E. H. Galvano- and thermo-magnetic coefficients for a multi-band conductor. *J. Phys. C: Solid State Phys.* **1975**, *8*, 1837-1840.

(41) Andersen, H. L.; Zhang, J.; Yin, H.; Iversen, B. B. Structural stability and thermoelectric properties of cation- and anion-doped $Mg_2Si_{0.4}Sn_{0.6}$. *Inorg. Chem. Front.* **2017**, *4*, 456-467.

(42) Toberer, E. S.; May, A. F.; Snyder, G. J. Zintl chemistry for designing high efficiency thermoelectric materials. *Chem. Mater.* **2010**, *22*, 624-634.

(43) Harrison, J. W.; Hauser, J. R. Alloy scattering in ternary III-V compounds. *Phys. Rev. B* **1976**, *13*, 5347-5350.

(44) Goldsmid, H. J. *Thermoelectric Refrigeration*, Plenum, 1964.

(45) Kauzlarich, S. M.; Brown, S. R.; Jeffrey Snyder, G. Zintl phases for thermoelectric devices. *Dalton Trans.* **2007**, 2099-2107.

(46) Ravich, Y. I.; Efimova, B. A.; Tamarchenko, V. I. Scattering of current carriers and transport phenomena in lead chalcogenides II. experiment. *Phys. Status Solidi B* **1971**, *43*, 453-469.

(47) Wang, H.; Schechtel, E.; Pei, Y.; Snyder, G. J. High thermoelectric efficiency of n-type PbS. *Adv. Energy Mater.* **2013**, *3*, 488-495.

(48) Klemens, P. G. Thermal resistance due to point defects at high temperatures. *Phys. Rev.* **1960**, *119*, 507-509.

(49) Callaway, J. Model for lattice thermal conductivity at low temperatures. *Phys. Rev.* **1959**, *113*, 1046-1051.

(50) Bhattacharya, S.; Chmielowski, R.; Dennler, G.; Madsen, G. K. H. Novel ternary sulfide thermoelectric materials from high throughput transport and defect calculations. *J. Mater. Chem. A* **2016**, *4*, 11086-11093.

(51) Chmielowski, R.; Bhattacharya, S.; Xie, W.; Pere, D.; Jacob, S.; Stern, R.; Moriya, K.;

Weidenkaff, A.; Madsen, G. K. H.; Dennler, G. High thermoelectric performance of tellurium doped paracostibite. *J. Mater. Chem. C* **2016**, *4*, 3094-3100.

TOC Entry:

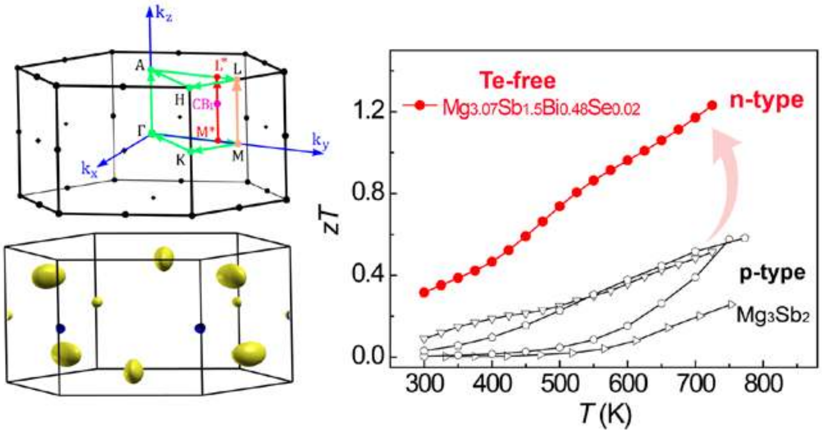
k_z
A
L*
L
H
CB1
M*
M
Γ
K
k_x
k_y
Te-free
Mg3.07Sb1.5Bi0.48Se0.02
n-type
p-type
Mg3Sb2
zT
0.0
0.4
0.8
1.2
300
400
500
600
700
800
T (K)